Experimental Correction of Arbitrary Instrument Functions in Optical Coherence Tomography Using Only Relative Measurements

Alexander A. Sovetsky, Alexander L. Matveyev, Lev A. Matveev, Peter A. Chizhov, and Vladimir Y. Zaitsev*

A.V. Gaponov-Grekhov Institute of Applied Physics of the Russian Academy of Sciences, 46 Uljanova str., Nizhny Novgorod 603950, Russian Federation

*e-mail: vyuzai@mail.ru

Abstract. One of recent trends in optical coherence tomography (OCT) is the development of various functional modalities beyond straightforward structural imaging. One of such modalities is extraction of optical attenuation coefficient (OAC) from OCT scans. The OAC distributions may be rather informative, however, their extraction from OCT scans can be seriously distorted by the instrument function of OCT setup which may seriously affect the observed depth-dependence of the OCT-signal amplitude. Various procedures for correcting the influence of the instrument function of the OCT setup on the estimated OAC distribution in the sample have been discussed in the literature. To introduce the corresponding correction factors theoretically such procedures, require sufficiently detailed knowledge of the OCT setup parameters. Alternative experimental methods make it possible to obviate the necessity of knowing the OCT-setup parameters, for example, by using a specially prepared calibration phantom with a known value of spatially uniform OAC. In this manuscript we propose an efficient experimental method which is based on exclusively relative measurements, for performing which neither OCT-setup parameters, nor absolute OAC value for the calibration phantom are required. The method makes it possible to correct instrument functions of arbitrary types in either spectral domain or time-domain OCT. Examples of application of the correction method for different OCT-setups are presented to emphasize that the use of uncorrected data may lead to rather strong errors of OAC-distribution estimation in both axial and lateral directions. The proposed method should be helpful to improve the diagnostic accuracy OCT examinations relying on the OAC extraction from OCT data.

Keywords: optical coherence tomography; optical attenuation coefficient; optical attenuation imaging; instrument function.

Paper #9285 received 23 Jun 2025; revised manuscript received 5 Jul 2025; accepted for publication 6 Jul 2025; published online 11 Sep 2025. doi: 10.18287/JBPE25.11.030301.

1 Introduction

One of main trends in Optical Coherence Tomography (OCT) in recent years is the development of new modalities (functional extensions) to complement conventional structural imaging [1]. In particular, such modalities as various realizations OCT-based angiography were developed [2−4], as well as OCT-based variants of elastography [5−8]. Other functional extensions of OCT are based on sophisticated analysis of speckle-pattern parameters (e.g., [9−11]). These modalities allow one to significantly increase the diagnostic value of OCT examinations.

Besides the above-mentioned modalities much attention has also been paid in recent years to the

development of OCT-based methods for estimation of optical attenuation coefficient (OAC) by analyzing the depth dependence of signal intensity in OCT scans (e.g. [12, 13]). The interest to OAC estimation was additionally stimulated in the last decade by study [14], where as elegant approach to reconstruction of depth-resolved OAC distribution was proposed for situations, in which the optical attenuation is dominated by scattering rather than by absorption. The latter situation is quite typical for biological tissues and OCT setups operating in the near-infrared range. Although the optical-signal attenuation for forward propagation of a plane wave in a spatially homogeneous medium is described by a simple exponential factor, estimation of the attenuation coefficient by analyzing the depth-dependence of signals in OCT scans is less trivial, even if it is known that the attenuation is strongly dominated by scattering. The point is that in OCT, besides the energy losses during the forth-and-back light propagation through the scattering tissue, the depth-dependence of the received signal is affected by a number of various factors, first of all, the influence of focusing (which may cause appreciable distortions even for not very large numerical apertures) and the sensitivity fall-off (or roll-off effect) intrinsic to spectral-domain OCT.

Even if the origin of such distortions is qualitatively clear [13−17], purely theoretical derivation of the correcting depth-dependent factors related to the focusing influence, sensitivity roll-off (and other instrument features) is challenging because all required parameters of the used OCT setup usually are not known in detail. As an alternative approach, experimental determining of the correcting depth-dependent factor could be made using a spatially homogeneous reference material with an *a priori* known OAC value. For example, Ref. [18] demonstrated the utilization of such a reference phantom in the form of diffuse-scattering homogeneous suspensions of polystyrene microspheres diluted in distilled water. Their optical properties were calculated using Mie theory for known refractive indices of water and polystyrene, known mean diameter of microspheres and standard deviation, as well as concentration of the microspheres in water. From these data, the scattering coefficient was calculated, the value of which was then compared with the slope of depth dependences of the OCT signal to estimate the correction depth-dependent profile.

Such determining of the correction profile involved more straightforward calculations of the scattering properties of the reference phantom in comparison with the theoretical correction of the instrument function of OCT setup, for which parameters usually are not sufficiently well known if known at all. Yet, even such simpler calculations of phantom scattering properties still require rather detailed knowledge of several parameters to sufficiently accurately predict the OAC for the reference-phantom. In view of this, it would be rather desirable to propose an experimental procedure of finding the correction profile, for which only relative calibration measurements would be sufficient without the necessity to know quantitative scattering properties of the phantom.

In this paper, we describe such a calibration procedure based on exclusively relative measurements and demonstrate its application to real OCT setups. To illustrate the efficiency of the proposed correction procedure, instructive examples are given to demonstrate the difference between the OAC estimates extracted with and without such preliminary calibration procedures.

2 Correction Procedure Principle

Generally speaking, the optical signal attenuation caused by energy losses due to scattering and absorption along the propagation path can be accounted for in a similar manner using exponential factors $\exp(-\mu_a z)$ and $\exp(-\mu_s z)$, where μ_a is the absorption coefficient, μ_s is the scattering coefficient and z is the propagation distance to the depth of the material. For a spatially-inhomogeneous material, the argument of the exponential function has an integral form, $\exp(-\mu_{a,s} z) \to \exp[-\int_0^z \mu_{a,s}) z')]dz'$. However, in OCT the depth-dependence of the received signal is not reduced to the simple exponential form because of the influence of several additional factors. If the intensity of the wave incident on the sample surface is J_0, then the intensity of the received signal can be represented in the following form [14, 18]:

$$I(z) = K \cdot J_0 F(z) S(z) \theta(z) \cdot \mu_s(z) \cdot \cdot \exp\{-2\int_0^z [\mu_s(z') + \mu_a(z')]dz'\}, \quad (2)$$

where coefficient K characterizes the reception sensitivity; function $F(z)$ describes the focusing influence (confocal function); depth-dependence $S(z)$ describes the sensitivity fall-off with increasing depth, which is typical for spectral-domain OCT systems. Function $\theta(z)$ describes the portion of the total scattered radiation propagated back from scatterers and collected over the receiving aperture.

Generally speaking, in biological tissues the optical signal attenuation is caused by combined action of scattering and absorption as in Eq. (2). However, usually the operating wavelength of OCT signals is chosen taking into account the so-called transparency windows of biotissues, in which the attenuation is minimal. In particular, near infra-red range is often chosen for creation OCT devices. For example, an often used wavelength in OCT is 1300 nm, for which numerous independent studies consistently indicate that in biological tissues the optical signal attenuation is strongly dominated by scattering rather that absorption ($\mu_a << \mu_s$), see, e.g., [19−21]. Under this condition for sufficiently small optical paths typical of OCT, in Eq. (2) it may be considered that the influence of absorption can be neglected and the exponential factor

$\exp\{-2\int_0^z[\mu_a(z')]dz'\}\to 1$. Then Eq. (2) reduces to a simpler form

$$I(z)=K\cdot J_0F(z)S(z)\theta(z)\cdot\mu_s(z)\cdot \cdot\exp\{-2\int_0^z\mu_s(z')dz'\}. \quad (3)$$

Then under the additional assumption that prefactor $F(z)S(z)\theta(z)$ in Eq. (3) is depth-independent an elegant method was proposed in Ref. [14] for finding the depth-resolved distribution of $\mu_s(z)$ of arbitrary form in the absence of additive measurement noises and in the case of complete decay of the observed signal intensity $I(z)$ within the visualized region:

$$\mu_s(z)=\frac{I(z)}{2\int_z^\infty I(z')dz'}. \quad (4)$$

However, while the assumptions about $\exp\{-2\int_0^z[\mu_a(z')]dz'\}\to 1$ and the sufficiently strong scattering-induced decay of $I(z)$ within the visualization depth are fairly realistic in OCT, the assumption about depth independence of the instrument-related prefactor $F(z)S(z)\theta(z)=const$ is often appreciably violated and may seriously distort the reconstructed distribution $\mu_s(z)$ based on the use of Eq. (3). Thus, the raw measured dependence $I(z)$ should be somehow corrected to exclude the distorting influence of the depth-dependent prefactor $F(z)S(z)\theta(z)$.

For theoretical correction, the parameters of the OCT setup required to estimate the prefactor $F(z)S(z)\theta(z)$ are often insufficiently well known to the users. A natural alternative may be an experimental calibration method that could be used to find the correction profile $F(z)S(z)\theta(z)$ (in which possibly some other unknown distorting instrumental factors may enter).

At first glance, a good variant could be to perform calibration measurements using a phantom with an *a priori* uniform distribution of the scattering parameter $\mu_s=const$ and negligibly small absorption. In this case Eq. (2) reduces to a simpler form

$$I(z)=K\cdot J_0F(z)S(z)\theta(z)\cdot\mu_s\cdot\exp\{-2\mu_s z\}. \quad (5)$$

However, even if it is known that $\mu_s(z)=const$, still the unknown depth-dependent factor $\exp\{-2\mu_s\cdot z\}$ enters Eq. (5) and prevents the direct estimation of the sought profile $F(z)S(z)\theta(z)$. In view of this in work [18] the authors prepared a special phantom containing scattering microspheres with known optical parameters and concentration to find the factor $\exp\{-2\mu_s\cdot z\}$ by estimating μ_s of the prepared phantom from Mie theory. The advantage of this procedure is that it does not require knowing the OCT-system parameters. However, such a calibration method is rather laborious and requires special qualifications and components to prepare the calibration phantom with well controllable properties.

Thus, it is very desirable to develop an even simpler calibration method which requires neither knowledge of OCT-system parameters, nor parameter μ_s of the calibration sample, so that only relative measurements should be sufficient for determining the depth-dependent calibration profile.

To this end, one has to somehow exclude the unknown exponential factor $\exp\{-2\mu_s z\}$ in Eq. (5), so that purely relative measurements would suffice, even is μ_s is non-zero and unknown. These requirements can be achieved in the following measurement configuration shown in Fig. 1.

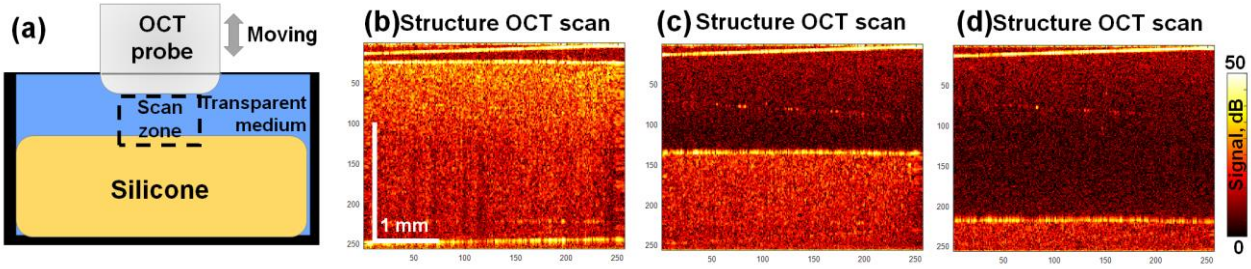

Fig. 1 Configuration of the calibration measurements with a non-scattering immersion medium placed between the OCT probe and the scattering sample, from which only the signal scattered from the near-surface region is analyzed. When the distance between the sample surface and the probe varies, the intensity of this signal is exclusively determined by the sought profile of the instrument function. (a) Schematic of the experiment; (b), (c) and (d) typical experimental scans for various distances between the silicone surface and the OCT probe of a spectral-domain OCT setup. Scans (b), (c) and (d) demonstrate that with increasing distance between the OCT probe and phantom the brightness of the phantom boundary and the near-surface region demonstrate noticeable decrease due to the influence of the sought instrument function.

In this configuration, instead of OCT-signal propagation in the bulk of a spatially uniform medium, it is proposed to acquire the backscattered optical signal from a near-surface layer of a laterally-homogeneous phantom sample. The sample surface should not be strongly scattering/reflecting to avoid the appearance of bright artefacts and overloading of the receiving system. For example, translucent silicones similar to those utilized as reference layers in compression optical coherence elastography [22−24] or sufficiently strongly scattering hydrogels [25] can be used. The sample should be gradually shifted (for example, upward from the bottom of the visualization zone towards the OCT probe) and the depth-dependent brightness of the sample surface should be acquired when the distance to the OCT probe is varied. The medium located above the surface of the gradually moving sample should be optically transparent. Consequently, in this configuration the functional form of the depth-dependent intensity $I_{cal}(z)$ of the received signal is determined exclusively by the sought combination $F(z)S(z)\theta(z)$ entering Eq. (4) before the exponential function. For compactness, this depth-dependent correction profile will be denoted $P_{corr}(z) = F(z)S(z)\theta(z)$. Notice that the pre-exponent depth-dependent multiplier $P_{corr}(z)$ may even comprise some other unknown instrument-dependent factors which would be also accounted for in the measured calibration dependence $I_{cal}(z)$ in the described experimental configuration.

Here, and in the above-presented equations we explicitly discuss only the OCT-probe motion along the axial coordinate *z* for given lateral coordinates. However, it is assumed that the OCT probe itself usually enables scanning in lateral directions (at least along one or both lateral coordinates), so that the described calibration procedures actually enable obtaining of a 2D or 3D map of the depth-dependent correction profiles.

It is important to emphasize an important requirement to such a calibration procedure, namely, the optically transparent medium between the OCT probe and the scattering phantom should have the refractive index close to that of the phantom imitating the biological tissue. Indeed, if the calibration would be performed in the non-absorbing air with $n = 1$, the so-found correction profile in air may noticeably differ from that in biotissues. A fairly good option is to use water with the refractive index $n = 1.33$ which is reasonably close to typical values of the refractive index of biotissues, $n = 1.35-1.4$. If necessary, some other liquid with the refractive index closer to that of biotissues may be used.

After obtaining the calibration dependence $I_{cal}(z)$ for gradually varying depth coordinate *z* (for each lateral coordinate of interest) in the experimental configuration shown in Fig. 1, the calibration profile $P_{corr}(z)$ for given lateral coordinate can be obtained by normalizing the raw dependence $I_{cal}(z)$ to the intensity in the chosen reference point, for example,

$$P_{corr}(z) = I_{cal}(z) / I_{cal}(0) . \qquad (6)$$

Such a calibration procedure does not require knowing the OCT setup parameters, as well as the scattering coefficient μ_s of the scattering phantom.

After dividing any other the intensity profile $I(z)$ described by Eq. (2) by the correction profile given by Eq. (6), $I(z) \to I(z) / P_{corr}(z)$, the depth dependence in Eq. (2) found with an unknown instrument function transforms to a simpler form

$$I_{corr}(z) = \bar{J}_0 \cdot \mu_s(z) \cdot \exp\{-2\int_0^z \mu_s(z')dz'\} , \qquad (7)$$

where $\bar{J}_0$ after such normalization gets somewhat different from the initial J_0 in Eq. (2), which does not prevent finding the unknown μ_s. For example, Vermeer's method [14] can be applied to the corrected profile $I_{corr}(z)$ given by Eq. (7) to find the depth-resolved OAC already cleaned from the distorting influence of the instrument factor.

It should also be noted that even if the immersion layer separating the phantom is non-scattering with $\mu_s \to 0$, still it may exhibit non-negligible absorption $\mu_a \neq 0$. For example, during the calibration the layer of transparent water without any scattering particles may introduce some signal attenuation described by the exponential factor $\exp(-2\mu_a z)$. However, the absorption parameter μ_a for water is well known in the entire optical range [26], as well as in the near infra-red range [27]. For example, according to Ref. [27], for 1.3 μm wavelength often used in OCT, the absorption parameter $\mu_a \approx 0.11$ 1/mm, so that for forth-and-back propagation within 1 mm depth, the absorption-induced reduction in the signal intensity is ~22% or ~0.9 dB, whereas the instrument function of OCT setups often varies by 15−30 dB within the same depth range. Therefore, although the contribution of absorption often may be much smaller than contributions of other factors, if necessary the absorption-related attenuation given by the factor $\exp(-2\mu_a z)$ can readily be introduced in Eq. (7) for the corrected intensity: $I_{corr}(z) \to I_{corr}(z)\exp(2\mu_a z)$.

In the next section we give some examples of utilization of the above described method, as well as compare results of OAC estimation using uncorrected and corrected OCT scans.

3 Experimental Examples of Correction Procedure Utilization

In this section we present results for two types (spectral-domain and time domain) OCT setups designed and produced in the Institute of Applied Physics RAS. Both OCT-setup types have a central wavelength of 1.3 μm, for which in biological tissues the observed attenuation is

strongly dominated by scattering rather than absorption. Consequently, Vermeer's approach [14] can be applied to OCT scans of those setups for obtaining depth-resolved OAC maps.

The first example shown in Fig. 2 is obtained for a spectral-domain OCT setup, for which several examples of OCT scans corresponding to various distances between the reference silicone surface and the OCT probe were shown in Fig. 1(b−d), where the bright slightly inclined line at the top of the scan is the boundary of the output window of the OCT probe. The darker region between the output glass of the probe and silicone surface is filled with immersing water by the above-discussed reasons. It is clear from the presented examples that the brightness of the near-surface region of the silicone phantom gradually decreases with increasing depth of the phantom. This fact is due to the instrument-function influence that we have to compensate. During the calibration measurement, a series of B-scans was acquired when an automated translation device gradually changed the distance between the OCT probe and the phantom. Then in each B-scan similar to those in Fig. 1(a−d) the position of the phantom surface and its intensity was automatically found for every A-scan. Then by combining the so-found positions and intensities of the phantom surface, a pseudo-B-scan was synthesized as shown in Fig. 2(a). Although the silicone was in average fairly uniform, random variations of the near-surface scattering intensity resulted in the appearance of a peculiar vertically-oriented streaky pattern in the synthesized pseudo-B-scan (Fig. 2(a)). Since this streaky structure was unrelated to the instrument-function influence, it was averaged within a sliding window 10×10 pixels in size. The resultant smoothed distribution is shown in Fig. 2(b). The pseudo-B-scan in Fig. 2(b) is subdivided in five vertical stripes with the boundaries marked by different colors. The respective five vertical profiles of OCT-signal intensity determined by the sought instrument function are shown by the corresponding colors in Fig. 2(c). If the instrument function was uniform, the signal intensity would not exhibit depth dependence. Thus, the so-found depth-dependent intensity dependence in each A-scans were used to obtain correction profiles via Eq. (6), for which the 2D map is presented in the color-coded form in Fig. 2(d). Notice that the signal intensity in Fig. 2(a) and 2(b) demonstrates a clear decrease caused by the combined influence of defocusing, the sensitivity roll-off and possibly by other instrument features typical of spectral-domain OCT systems. The total intensity decrease caused by the instrument function and yet unrelated to the signal attenuation reaches 15−20 dB within the visualized depth range (see the individual correction profiles in Fig. 2(c)). After application of the correcting profiles, the raw depth-dependent OCT signals are transformed to the corrected form corresponding to Eq. (7) after which the spatially-resolved maps of the optical attenuation coefficient could be obtained using Vermeer's approach [14]. When necessary, the correction for the presence of noise and incomplete decay of the OCT signal within the visualization depth could be introduced as discussed in Refs. [14, 28].

It is visible in Fig. 2 (especially in Panel (a)) that the trajectories of scatterers look slightly inclined from the vertical direction. This is caused by the slight inclination of the output-glass surface of the OCT probe, which is often introduced in spectral-domain setups to mitigate artefacts caused by light reflections from parallel surfaces of the optical elements of OCT probes. It made no sense to specially correct this small inclination so that the correction profile map in Fig. 4(d) was represented within the rectangular region. It can be noted that some OCT probes may use tilting optical beam for enabling lateral scanning, so that the resultant scans acquire sector shape similar to that for ultrasound medical scans. In the latter case the reconstructed instrument function map would also have a sector shape.

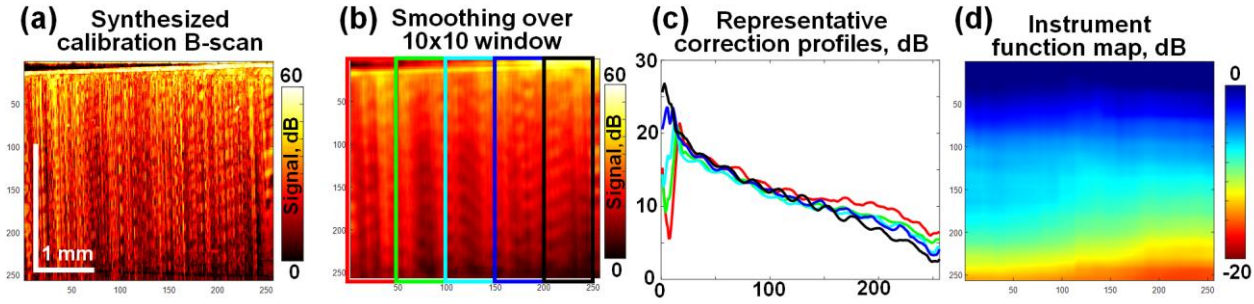

Fig. 2 Application of the calibration procedure to a spectral-domain OCT setup, for which examples of OCT scans are shown in Fig. 1(b−d). Panel (a) shows the synthesized pseudo-B-scan corresponding to the gradually varying distance between the OCT-probe and phantom surface with immersion water layer placed between them as shown in Fig. 1. Panel (b) is the same pseudo-B-scan smoothed using a sliding averaging window 10×10 pixels in size; panel (c) shows 5 representative correction profiles for 5 vertical regions with the boundaries marked by the respective colors; panel (d) is the summarizing 2D map of the so-found correction profiles normalized to the unity value at the surface of the scan using Eq. (6).

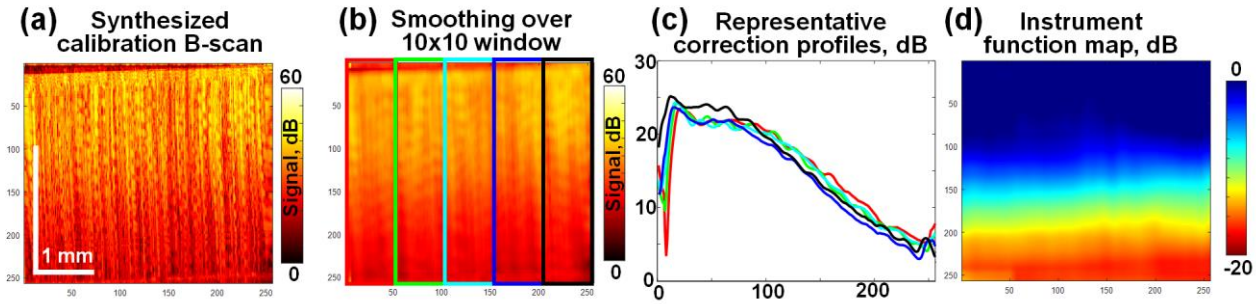

Fig. 3 Application of the calibration procedure to the same spectral-domain OCT setup as in Fig. 2, but preformed in air without the immersion water layer. Panel (a) shows the synthesized pseudo-B-scan corresponding to the gradually varying distance between the OCT-probe and phantom surface in air; (b) the same pseudo-B-scan smoothed using a sliding averaging window 10×10 pixels in size; panel (c) shows 5 representative correction profiles for 5 vertical regions with the boundaries marked by the respective colors in panel (b); (d) the summarizing 2D map of correction profiles normalized to the unity value at the surface of the scan via Eq. (6).

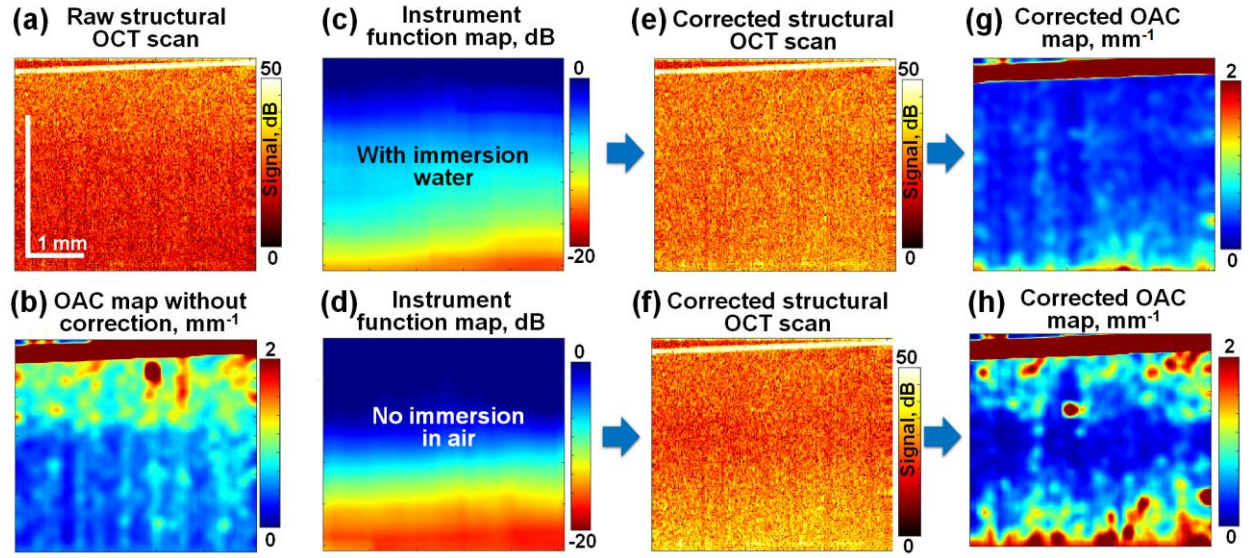

Fig. 4 Comparison of OAC maps derived from scans of a homogeneous silicone sample using the same OCT setup as in Fig. 2 without and with correction for the distorting influence of the instrument function. (a) The raw structural scan; (b) the OAC map derived directly from the initial structural scan without any correction; (c) the map of correction profiles obtained using the immersion water layer above the silicone sample and (d) the correction-profile map obtained for the same silicone phantom in air; (e) and (f) the corrected structural scans for the correction-profile map (c) obtained with immersion water layer and map (d) obtained without immersion in air, respectively; (g) and (h) the corresponding corrected OAC maps.

The next Fig. 3 also shows the results of the calibration procedure for the same OCT setup, but in contrast to Fig. 2 the calibration is performed in air without the immersion water layer between the phantom surface and OCT probe. It is clear that in the absence of the immersion layer the focus depth experienced noticeable axial shift, so that the individual calibration profiles in Fig. 3(c) and the summarizing 2D map of the correction profiles in Fig. 3(d) demonstrate well visible difference from their counterparts in Fig. 2(c) and 2(d).

The comparative results of OAC-map reconstruction without any correction and with application correction-profile maps (instrumental functions) obtained either using the immersion water layer (like in Fig. 2) or in air (like in Fig. 3) are demonstrated in Fig. 4. Figure 4(b) demonstrates that the OAC map found without any correction of the instrument function exhibits well-visible artefactual depth dependence (clearly elevated OAC in the upper part of the scan, although the phantom silicone sample is homogeneous). Figures 4(e) and 4(f) show the structural OCT scans obtained from the raw scan in Fig. 4(a) by applying the correction profiles obtained through the immersion layer (Fig. 4(c)) and in air without immersion (Fig. 4(d)). The corrected scans demonstrate more homogeneous intensity distribution than the raw scan in Fig. 4(a), which means that it is mostly the influence of the instrument function rather than scattering-related losses which caused the $I(z)$ decrease visible in Fig. 4(a) for larger depths. Figure 4(g) derived from the corrected scan from Fig. 4(e) for the

instrument function correctly found with immersion layer demonstrates much more homogenous OAC distribution than the uncorrected OAC map in Fig. 4(b). Finally, Fig. 4(h) shows the OAC map for the incorrect calibration procedure performed in air. In this case the OAC map again shows pronounced artefactual inhomogeneities, although this artefactual inhomogeneity differs from that in Fig. 4(b) obtained without any correction. In all cases in Fig. 4 the OAC maps are reconstructed using the spatially-resolved Vermeer's method (with accounting of noise and incomplete decay [28]). These examples demonstrate high efficiency of the proposed calibration procedure, correctly performed with immersion.

The next example shown in Fig. 5 relates to another OCT system with is time-domain rather than spectral-domain OCT. It has another type of flexible endoscopic probe with a laterally narrower visualization field. The results of utilization of similar calibration procedures are demonstrated in Fig. 5.

Figure 5(a) shows the initial B-scan for the same silicone phantom as in the previous figures. The uncorrected OAC map directly derived from the raw B-scan is shown in Fig. 5(b) with the artefactual elevated OAC-level in the central part of the scan. The correction-profile map obtained though the immersion water layer is shown in Fig. 5(c) and demonstrates pronounced dependence not only in the axial but also in the lateral direction with pronounced right-left asymmetry. The latter fact would be hardly possible to take into account in theoretical expressions but experimentally this complex form of the calibration function is readily reconstructed. The corrected structural OCT scan and the derived OAC map found after application of the instrument function from Fig. 5(c) are shown in Figs. 5(d) and 5(e), respectively. The OAC again is reconstructed using Vermeer's approach with correction for the incomplete decay according to approach [28], the application of this approach is well justified for the used homogeneous sample. As expected, the post-correction OAC distribution in Fig. 5(e) is appreciably more homogeneous in contrast to the uncorrected OAC in Fig. 5(b), where the inhomogeneity of the instrument function results in the appearance of artefactual increased OAC in the vicinity of focal region. Therefore, the presented examples for both spectral-domain and time-domain OCT setups demonstrate the operability and efficiency of the proposed calibration procedures. Moreover, even asymmetric forms of instrument functions can be readily found using the same procedures.

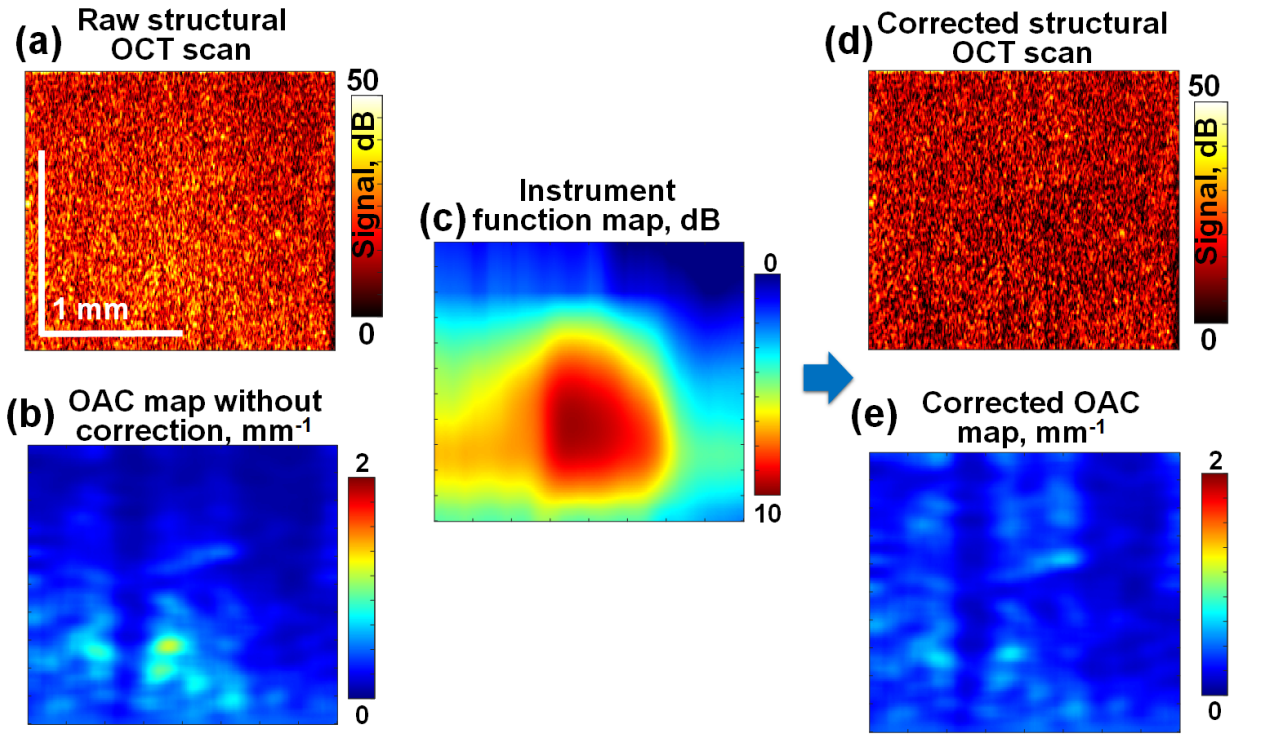

Fig. 5 Demonstration of the correction procedure applied to a time-domain OCT device. (a) The raw B-scan of a spatially homogeneous silicone sample and (b) the reconstructed OAC map based Vermeer's approach [14] (with correction for incomplete signal decay and noise background [28], but without correction for the instrument function). (c) the instrument function reconstructed by the proposed method, (d) corrected structural OCT scan obtained from the initial scan (a) using the instrument function (c); (e) the corrected OAC map, in which the artefactual inhomogeneities of OAC visible in the uncorrected OAC map (d) are significantly suppressed. Notice that in this example for the time-domain OCT the correction profile is increasing at larger depths due to pronounced influence of focusing (see the increased signal intensity in the lower part of panel (a)). This is in contrast to the correction profiles decreasing at larger depths that were shown in Fig. 2 for the spectral domain OCT.

4 Conclusions

In view of rather promising diagnostic prospects, OCT-based estimation of optical attenuation attracts increasing attention of researches. The corresponding studies concern both particular diagnostic applications of OAC in biomedical problems (e.g., [29−31]), as well as further development/perfection of OAC estimation methods [12−15, 18]. Special attention is paid to the adequate accounting and compensation of possible distortions in the reconstructed OAC maps caused by the instrument function of the OCT setup. In particular, the role of OCT-beam focusing and the sensitivity loss (roll-off effect) typical of spectral-domain OCT systems is widely discussed in the literature [12−14]. However, theoretical expressions accounting for the influence of such instrument-related effects require sufficiently complete knowing of the OCT-setup parameters, which is not always possible. In view of this, alternative experimental methods of obtaining correction profiles for OAC estimation are of evident importance. An instructive example is Ref. [18], where the correction profile was determined by utilizing a specially prepared homogeneous phantom with known scattering properties predicted using Mie theory.

However, since creation of phantoms with controllable properties is rather non-trivial and laborious task, it is very desireable to develop a simpler experimental approach, for which absolute values of a phantom sample are not required at all and purely relative measurements are sufficient. In this study we described such a simple but efficient experimental method for obtaining correction profiles to determine the unknown instrument function of OCT setup using only relative measurements. We demonstrated that it can be equally applied to either spectral-domain or time-domain OCT setups. Even insufficiently known construction features of OCT setup resulting in lateral inhomogeneity of the sought depth-dependent correction profiles can also be readily accounted for using the proposed calibration method. Also unknown depth-dependent coefficients (that may be introduced in the OCT setup by the manufactures to improve the visual impression of the ontained scan) would also be eliminated by the described method for correct estimation of OAC. Thus, the proposed approach and above presented demonstrations of its efficiency for improvement of OAC reconstruction from OCT scans should be very beneficial for a broad range of diagnostic applications of multimodal OCT.

Acknowledgement

The study was supported by the Russian Science Foundation (grant No. 22-12-00295-П).

Disclosures

All authors declare that there is no conflict of interest in this paper.

References

1. R. Leitgeb, F. Placzek, E. Rank, L. Krainz, R. Haindl, Q. Li, M. Liu, M. Andreana, A. Unterhuber, T. Schmoll, and W. Drexler, "Enhanced medical diagnosis for dOCTors: a perspective of optical coherence tomography," Journal of Biomedical Optics 26(10), 100601 (2021).
2. A. Mariampillai, B. A. Standish, E. H. Moriyama, M. Khurana, N. R. Munce, M. K. K. Leung, J. Jiang, A. Cable, B. C. Wilson, I. A. Vitkin, and V. X. D. Yang, "Speckle variance detection of microvasculature using swept-source optical coherence tomography," Optics Letters 33(13), 1530 (2008).
3. A. Zhang, Q. Zhang, C.-L. Chen, and R. K. Wang, "Methods and algorithms for optical coherence tomography-based angiography: a review and comparison," Journal of Biomedical Optics 20(10), 100901 (2015).
4. A. Moiseev, S. Ksenofontov, M. Sirotkina, E. Kiseleva, M. Gorozhantseva, N. Shakhova, L. Matveev, V. Zaitsev, A. Matveyev, E. Zagaynova, V. Gelikonov, N. Gladkova, A. Vitkin, and G. Gelikonov, "Optical coherence tomography-based angiography device with real-time angiography B-scans visualization and hand-held probe for everyday clinical use," Journal of Biophotonics 11(10), e201700292 (2018).
5. K. V. Larin, D. D. Sampson, "Optical coherence elastography – OCT at work in tissue biomechanics [Invited]," Biomedical Optics Express 8(2), 1172 (2017).
6. V. Y. Zaitsev, A. L. Matveyev, L. A. Matveev, A. A. Sovetsky, M. S. Hepburn, A. Mowla, and B. F. Kennedy, "Strain and elasticity imaging in compression optical coherence elastography: The two-decade perspective and recent advances," Journal of Biophotonics 14(2), e202000257 (2021).
7. M. A. Kirby, I. Pelivanov, S. Song, Ł. Ambrozinski, S. J. Yoon, L. Gao, D. Li, T. T. Shen, R. K. Wang, and M. O'Donnell, "Optical coherence elastography in ophthalmology," Journal of Biomedical Optics 22(12), 1 (2017).
8. E. V. Gubarkova, A. A. Sovetsky, L. A. Matveev, A. L. Matveyev, D. A. Vorontsov, A. A. Plekhanov, S. S. Kuznetsov, S. V. Gamayunov, A. Y. Vorontsov, M. A. Sirotkina, N. D. Gladkova, and V. Y. Zaitsev, "Nonlinear elasticity assessment with optical coherence elastography for high-selectivity differentiation of breast cancer tissues," Materials 15(9), 3308 (2022).
9. D. Zhu, J. Wang, M. Marjanovic, E. J. Chaney, K. A. Cradock, A. M. Higham, Z. G. Liu, Z. Gao, and S. A. Boppart, "Differentiation of breast tissue types for surgical margin assessment using machine learning and polarization-sensitive optical coherence tomography," Biomedical Optics Express 12(5), 3021 (2021).

10. M. Niemczyk, D. R. Iskander, "Statistical analysis of corneal OCT speckle: a non-parametric approach," Biomedical Optics Express 12(10), 6407 (2021).
11. L. A. Matveev, A. A. Sovetsky, A. L. Matveyev, I. A. Vitkin, M. Assaad, and V. Y. Zaitsev, "Refined speckle contrast estimation in OCT based on compensation of scattering-related distortions of speckle pattern parameters," Laser Physics Letters 22(1), 015601 (2025).
12. S. Chang, A. K. Bowden, "Review of methods and applications of attenuation coefficient measurements with optical coherence tomography," Journal of Biomedical Optics 24(09), 1 (2019).
13. P. Gong, M. Almasian, G. Van Soest, D. M. De Bruin, T. G. Van Leeuwen, D. D. Sampson, and D. J. Faber, "Parametric imaging of attenuation by optical coherence tomography: review of models, methods, and clinical translation," Journal of Biomedical Optics 25(04), 1 (2020).
14. K. A. Vermeer, J. Mo, J. J. A. Weda, et al.H. G. Lemij, and J. F. De Boer, "Depth-resolved model-based reconstruction of attenuation coefficients in optical coherence tomography," Biomedical Optics Express 5(1), 322 (2014).
15. B. Ghafaryasl, K. A. Vermeer, J. Kalkman, T. Callewaert, J. F. De Boer, and L. J. Van Vliet, "Analysis of attenuation coefficient estimation in Fourier-domain OCT of semi-infinite media," Biomedical Optics Express 11(11), 6093 (2020).
16. E. P. Sherstnev, P. A. Shilyagin, D. A. Terpelov, V. M. Gelikonov, and G. V. Gelikonov, "An improved analytical model of a spectrometer for optical coherence tomography," Photonics 8(12), 534 (2021).
17. A. A. Sovetsky, A. L. Matveyev, L. A. Matveev, P. A. Chizhov, and V. Y. Zaitsev, "Simple "Digital Phantom" for testing attenuation-imaging methods in optical coherence tomography," Journal of Biomedical Photonics & Engineering 10(2), 020302 (2024).
18. L. Scolaro, R. A. McLaughlin, B. R. Klyen, B. A. Wood, P. D. Robbins, C. M. Saunders, S. L. Jacques, and D. D. Sampson, "Parametric imaging of the local attenuation coefficient in human axillary lymph nodes assessed using optical coherence tomography," Biomedical Optics Express 3(2), 366 (2012).
19. V. V. Tuchin, D. Zhu, and E. A. Genina (Eds.), "Handbook of tissue optical clearing: new prospects in optical imaging: New Prospects in Optical Imaging," CRC Press, Boca Raton (2021). eBook ISBN: 9781003025252.
20. V. V. Tuchin, "Tissue optics and photonics: light-tissue interaction," Journal of Biomedical Photonics & Engineering 1(2), 98–134 (2015).
21. F. Bergmann, F. Foschum, L. Marzel, and A. Kienle, "*Ex Vivo* determination of broadband absorption and effective scattering coefficients of porcine tissue," Photonics 8(9), 365 (2021).
22. V. Y. Zaitsev, A. L. Matveyev, L. A. Matveev, E. V. Gubarkova, A. A. Sovetsky, M. A. Sirotkina, G. V. Gelikonov, E. V. Zagaynova, N. D. Gladkova, and A. Vitkin, "Practical obstacles and their mitigation strategies in compressional optical coherence elastography of biological tissues," Journal of Innovative Optical Health Sciences 10(06), 1742006 (2017).
23. E. V. Gubarkova, E. B. Kiseleva, M. A. Sirotkina, D. A. Vorontsov, K. A. Achkasova, S. S. Kuznetsov, K. S. Yashin, A. L. Matveyev, A. A. Sovetsky, L. A. Matveev, A. A. Plekhanov, A. Y. Vorontsov, V. Y. Zaitsev, and N. D. Gladkova, "Diagnostic OCT and OCT-Elastography for differentiation of breast cancer subtypes: comparative study," Diagnostics 10(12), 994 (2020).
24. A. A. Sovetsky, A. L. Matveyev, L. A. Matveev, G. V. Gelikonov, and V. Y. Zaitsev, "Mapping large strains in phase-sensitive OCT: Key role of supra-pixel displacement tracking in incremental strain evaluation," Journal of Biomedical Photonics & Engineering 8(3), 030304 (2022).
25. Y. M. Alexandrovskaya, E. M. Kasianenko, A. A. Sovetsky, A. L. Matveyev, and V. Y. Zaitsev, "Spatio-temporal dynamics of diffusion-associated deformations of biological tissues and polyacrylamide gels observed with optical coherence elastography," Materials 16(5), 2036 (2023).
26. C. K. N. Patel, A. C. Tam, "Optical absorption coefficients of water," Nature 280(5720), 302–304 (1979).
27. C.-L. Tsai, J.-C. Chen, and W.-J. Wang, "Near-infrared absorption properties of biological soft tissue constituents," Journal of Medical and Biological Engineering 21(1), 7–14 (2001).
28. J. Liu, N. Ding, Y. Yu, X. Yuan, S. Luo, J. Luan, Y. Zhao, Y. Wang, and Z. Ma, "Optimized depth-resolved estimation to measure optical attenuation coefficients from optical coherence tomography and its application in cerebral damage determination," Journal of Biomedical Optics 24(03), 1 (2019).
29. P. Gong, S. Es'haghian, K.-A. Harms, A. Murray, S. Rea, F. M. Wood, D. D. Sampson, and R. A. McLaughlin, "In vivo label-free lymphangiography of cutaneous lymphatic vessels in human burn scars using optical coherence tomography," Biomedical Optics Express 7(12), 4886 (2016).
30. A. Moiseev, E. Sherstnev, E. Kiseleva, K. Achkasova, A. Potapov, K. Yashin, M. Sirotkina, G. Gelikonov, V. Matkivsky, P. Shilyagin, S. Ksenofontov, E. Bederina, I. Medyanik, E. Zagaynova, and N. Gladkova, "Depth-resolved method for attenuation coefficient calculation from optical coherence tomography data for improved biological structure visualization," Journal of Biophotonics 16(12), e202100392 (2023).
31. A. A. Sovetsky, K. S. Yashin, R. D. Zinatullin, A. L. Matveyev, V. Y. Zaitsev, and L. A. Matveev, "Optical coherence tomography-based in vivo automatic detection of brain tissue malignancy using optical attenuation coefficient and refined speckle contrast: preliminary results," Laser Physics Letters 22(6), 065601 (2025).